DOI: 10.1002/ ((please add manuscript number))
Article type: Full Paper

Amorphous Dual-layer Coating: Enabling High Li-ion Conductivity of Non-sintered Garnet-type Solid Electrolyte

Yuan Gao, Shuyang Sun, Xin Zhang, Yongfeng Liu, Jianjiang Hu, Zhenguo Huang, Mingxia Gao, and Hongge Pan*

Y. Gao, S. Y. Sun, Dr. X. Zhang, Prof. Y. F. Liu, Prof. M. X. Gao, Prof. H. G. Pan
State Key Laboratory of Silicon Materials and School of Materials Science and Engineering, Zhejiang University, Hangzhou 310027, China
E-mail: mselyf@zju.edu.cn
Prof. J. J. Hu
School of Chemistry and Chemical Engineering, Yantai University, Yantai 264005, China
Prof. Z. G. Huang
School of Civil & Environmental Engineering, University of Technology Sydney, 81 Broadway, Ultimo, NSW, 2007, Australia

Keywords: energy storage materials, rechargeable Li batteries, solid state electrolyte, borohydrides, LLZTO

Abstract:

Garnet-type oxide $Li_{6.4}La_3Zr_{1.4}Ta_{0.6}O_{12}$ (LLZTO) has attracted considerable attention as a highly promising solid state electrolyte. However, its high ionic conductivity is achievable only after high temperature sintering (~1200 ºC) to form dense pellets but with detrimental brittleness and poor contact with electrodes. Herein, we demonstrate a novel strategy to achieve high Li^+ ion conductivity of LLZTO without sintering. This was realized by ball milling LLZTO together with $LiBH_4$, which resulted in a LLZTO composite with unique amorphous dual coating: $LiBO_2$ as the inner layer and $LiBH_4$ as the outer layer. After cold pressing the LLZTO composite powders under 300 MPa to form electrolyte pellets, a high Li^+ ion conductivity of 8.02×10^{-5} S cm^{-1} was obtained at 30 ºC, which is four orders of magnitude higher than that of the non-sintered pristine LLZTO pellets (4.17×10^{-9} S cm^{-1}). The composite electrolyte displays an ultrahigh Li^+ transference number of 0.9999 and enables symmetric Li-Li cells to be cycled for 1000 h at 60 ºC and 300 h at 30 ºC. The significant improvements are attributed to the

continuous ionic conductive network among LLZTO particles facilitated by $LiBH_4$ that is chemically compatible and electrochemically stable with Li metal electrode.

1. Introduction

The rapid development of electronic devices and electric vehicles raises the demand for batteries with high energy density, long cycling life and better safety.[1] All solid-state batteries (ASSBs) have therefore attracted significant attention because solid state electrolytes (SSEs) enhance safety and overall electrochemical performance.[2] Several types of compounds have been investigated as SSEs including oxides, sulfides and hydrides.[3] Among them, the garnet-type oxide $Li_7La_3Zr_2O_{12}$ (LLZO) and its derivatives hold great promise because of their high ionic conductivity and good chemical stability.[4] In particular, Ta-doped LLZO ceramic electrolyte (LLZTO) delivers a Li^+ ion conductivity of 10^{-4} - 10^{-3} S cm^{-1} at ambient temperature, which is much higher than LLZO and even comparable to traditional liquid electrolytes.[5] However, the LLZTO electrolyte does not readily integrate with Li metal anode due to an incompact structure arising from its extremely high Young's modulus (150 GPa) and the poor interface contact between LLZTO and Li metal.[6] Dense ceramic pellets need to be prepared by high-pressure compression followed by sintering at high temperatures (~ 1200 ºC),[7] which is time consuming and energy intensive. In addition, the sintered ceramic pellets are usually thick and fragile, and difficult for upscaled applications.[8]

Considerable efforts have been devoted to improving the applicability of LLZTO by reducing the sintering temperatures and/or blending with polymers. For example, oxides such as Li_3BO_3, SiO_2 and $La_2Zr_2O_7$, were employed as sintering aids to bridge the grain boundaries and improve densification at lowered sintering temperatures.[9-11] An 28% increase in the relative density was achieved for LLZTO after introducing 1 mol% SiO_2.[10] Similar phenomenon was also observed for LLZTO electrolyte mixed with $La_2Zr_2O_7$ by promoting the formation of glass-like phases binding LLZTO grains.[11] However, high temperature sintering is still necessary for the

preparation of solid electrolyte pellets. LLZTO-polymer composite electrolytes have also been studied by embedding LLZTO powders into polymer matrices, which offer advantages including good processability, lightweight and good contact with electrodes.[12,13] However, their Li^+ transference numbers are relatively low (below 0.8) due to the inert polymer matrices, and heating treatment above 150 ºC is still needed to melt the polymers to form composite electrolytes.

Recently, surface engineering proves effective to improve the density of electrolyte pellets with reduced interface resistance and enhanced ionic conductivity at lower sintering temperatures.[7b,14] Tian et al. fabricated a LLZTO composite electrolyte coated with amorphous Li_3OCl by melting-quenching at 350 ºC.[14] The amorphous Li_3OCl worked as a binder and bridge to fill the voids of LLZTO pellets. In another study, LiCl-coated LLZTO electrolyte pellets exhibited three orders of magnitude higher ionic conductivity than pristine LLZTO, but their preparation involved water or ethanol solutions which needs to be removed before use.[7b] So far, no success has been reported in achieving both high ionic conductivity and high Li^+ transference number for LLZTO pellets prepared merely by cold pressing without sintering.

In this work, we report for the first time a scalable method to engineer the surface of LLZTO particles to achieve high ionic conductivity and good electrochemical properties. This was realized simply by ball milling LLZTO with $LiBH_4$, leading to the formation of a unique LLZTO composite that was two-fold coated with amorphous boron compounds, i.e., $LiBO_2$ as the inner and $LiBH_4$ as the outer coating. After cold pressing under 300 MPa, a SSE of the LLZTO composite with high Li^+ ion conductivity (8.02×10^{-5} S cm^{-1}) at 30 ºC was obtained. An ultrahigh Li^+ transference number of 0.9999 as well as a wide electrochemical window (6 V vs. Li / Li^+) were achieved. A symmetric Li|LLZTO-4$LiBH_4$|Li cell was cycled stably at 60 ºC for more than 1000 h and at 30 ºC for more than 300 h at 0.15 mA cm^{-2}. Our work opens a new possibility to practically apply non-sintered garnet-type LLZTO composite electrolyte for high-performance ASSLBs.

2. Results and Discussion

2.1 Preparation and characterization of the LLZTO composite electrolyte.

The dual amorphous layer-coated LLZTO composite was prepared by ball milling LLZTO and $LiBH_4$ on a planetary ball mill (**Figure 1**a). H_2 was detected in the gases evolved during ball milling by mass spectrometric (MS) analysis (**Figure S1**, Supporting Information), which indicates a reaction between LLZTO and $LiBH_4$. The resultant solid-state products were characterized by X-ray diffraction (XRD), electronic paramagnet resonance (EPR), Fourier transform infrared (FTIR) spectroscopy, scanning electron microscopy (SEM), transmission electron microscopy (TEM), energy dispersive X-ray spectroscopy (EDS) and X-ray photoelectron spectroscopy (XPS). **Figure 1**b and c show the XRD patterns and FTIR spectra of the milled LLZTO-*x*$LiBH_4$ samples. XRD patterns reveal only the cubic phase LLZO (PDF No. 01-080-6143) **(Figure 1**b), whereas no phase related to $LiBH_4$ could be indexed, even for the LLZTO-8$LiBH_4$ sample, implying that boron-containing species became amorphous. Careful comparison reveals a slight low-angle shifting for the strongest reflection (4 2 2) of LLZTO with increasing the $LiBH_4$ amount, indicating an increase in the lattice parameters. The EPR measurement identifies the presence of oxygen vacancies from a strong signal around 3500 G (**Figure 1**c).[15] This was further evidenced by the formation of low-valence Zr and Ta as characterized by high-resolution XPS (**Figure 1**d). We therefore believe that the oxygen vacancies were created in the LLZTO structure after reacting with $LiBH_4$, which explains reasonably the slightly larger lattice parameters.[1d,16] The characteristic IR bands of B-H vibration in $LiBH_4$ at 2386, 2293, 2226 and 1127 cm^{-1} were visible,[17] especially for samples with high $LiBH_4$ contents (**Figure 1**e). In addition, the IR band position at 1442, 879, 763 and 692 cm^{-1} assignable to B-O vibrations were discernable, pointed to the formation of $LiBO_2$.[18] These results indicate that the resultant solid-state products were composed of oxygen vacancy-rich LLZTO, $LiBO_2$ and $LiBH_4$. Obviously, $LiBH_4$ with strong reducing capability reacted with

LLZTO, initiated by energetic collisions between milling balls, forming $LiBO_2$ and oxygen vacancy-rich LLZTO.

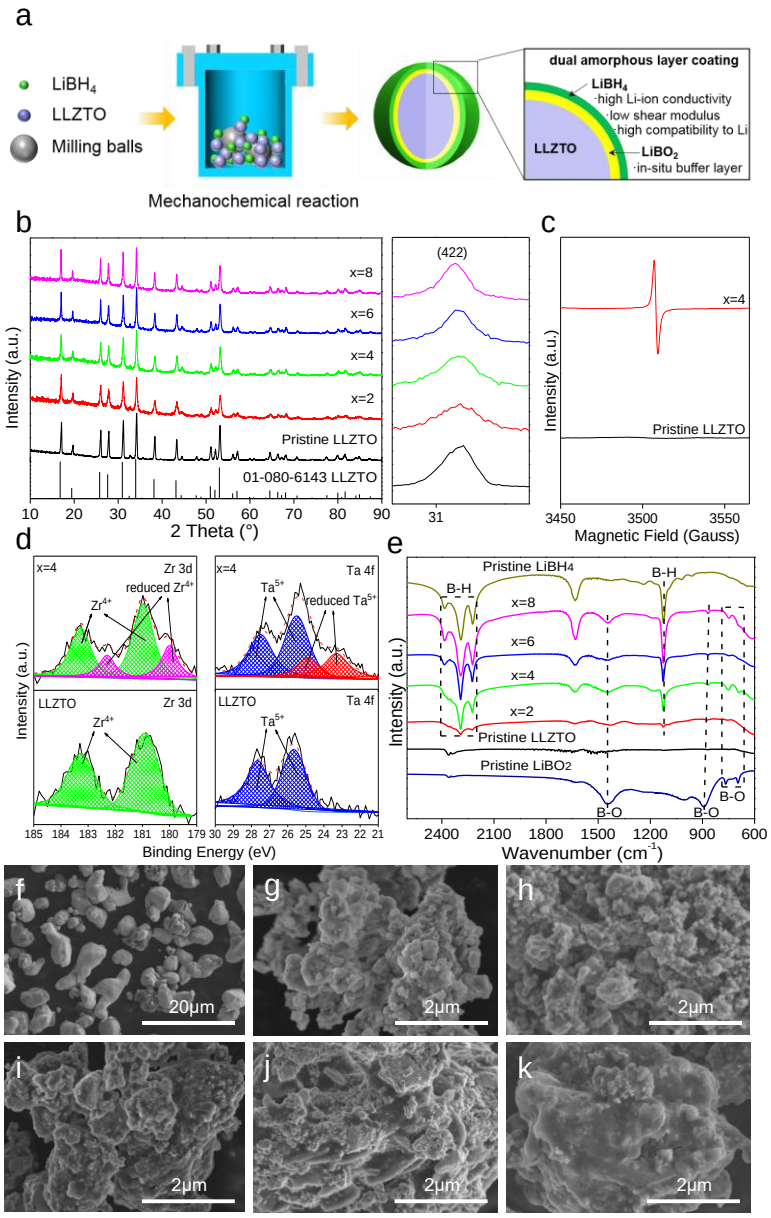

Figure 1. a) Schematic of the preparation of $LiBH_4$-modified LLZTO. b) XRD patterns, c) EPR, d) high resolution XPS spectra of Zr 3d and Ta 4f and e) FTIR spectra of the milled LLZTO-*x*$LiBH_4$ samples. SEM images of f) LLZTO raw material and the milled LLZTO-*x*$LiBH_4$ samples for g) x = 0, h) x = 2, i) x = 4, j) x = 6 and k) x = 8.

Figure 1f-k present the SEM images of pristine LLZTO and as-milled LLZTO-*x*$LiBH_4$ samples. Pristine LLZTO particles appear irregular in shape and the particle sizes range from 5

to 10 μm (**Figure 1**f). Ball milling effectively pulverized the particles which became smaller than 5 μm in size (**Figure 1**g). The introduction of $LiBH_4$ during ball milling leads to the aggregation and adhesion of particles (**Figure 1**h-k), which even exhibit encapsulation-like morphology for the sample at $x = 8$. This is possibly due to the low Young's modulus of $LiBH_4$ and newly formed $LiBO_2$ enabling coatings around hard LLZTO particles, which would improve the processability and formability of LLZTO under cold-pressing treatment.

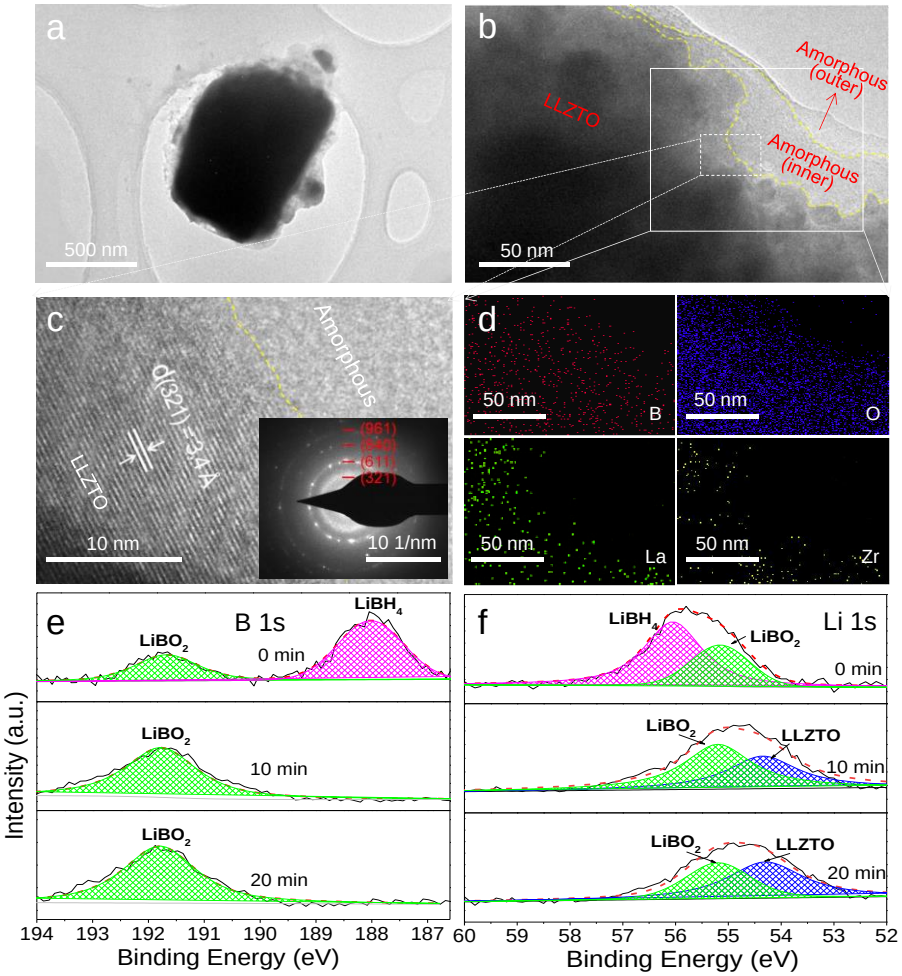

Figure 2. a, b) TEM, c) HRTEM images and d) the corresponding EDS mapping images of the as-milled LLZTO-4$LiBH_4$ sample. The inset of c) is the SAED pattern. High resolution XPS spectra of e) B 1s and f) Li 1s of the LLZTO-4$LiBH_4$ sample before and after sputtering.

Further TEM observations reveal a two-fold coating on LLZTO particles for the $LiBH_4$-containing sample (**Figure 2**a and b). The high-resolution TEM (HRTEM) image (**Figure 2**c)

presents amorphous coating and fringes with interplanar spacings of 0.34 nm for the core corresponding to (321) crystal plane of LLZTO. EDS mapping indicates that element B concentrates on the surface while La and Zr are in the inner core (**Figure 2**d). EDS point analyses also prove that B dominates points 1 and 2 at the surface while the relative contents of La, Zr, Ta and O are significantly higher for point 3 in the inner (**Figure S2**, Supporting Information). This indicates that after ball milling the LLZTO particles are covered by B-containing amorphous layers.

Figure 2e and f show the XPS depth profile of element B and Li in LLZTO-4$LiBH_4$ (the sample with the highest SSE performance, discussion in the following sections) before and after sputtering. The high-resolution B 1s XPS spectrum (**Figure 2**e) exhibits the typical binding energy of B(-H) in $LiBH_4$ at 187.8 eV before sputtering.[19] After sputtering for 10 min and 20 min, a new B 1s XPS peak corresponding to B(-O) in $LiBO_2$ at 191.7 eV was observed along with the disappearance of $LiBH_4$.[20] For the high-resolution Li 1s XPS spectra of the milled sample (**Figure 2**f), there are two Li 1s peaks with the stronger one at 56.2 eV attributed to $LiBH_4$ and the weaker one at 55.2 eV attributed to $LiBO_2$. After 10 minutes of sputtering, the Li 1s peak belonging to LLZTO at 54.5 eV appeared,[21] and that of $LiBH_4$ disappeared. Further increasing the sputtering time to 20 min, the relative intensity of Li 1s peak of LLZTO increased, while that of $LiBO_2$ weakened. This clearly demonstrates that the amorphous coating is a dual-layer structure consisting of $LiBH_4$ as the outer and $LiBO_2$ as the inner layer. Here, the *in-situ* formation of $LiBO_2$ in immediate contact with LLZTO serves as a buffer layer to prevent further reaction between $LiBH_4$ and LLZTO during ball milling. A reasonable evidence is that the content of newly formed $LiBO_2$ increased gradually with ball milling time and basically stabilized when approaching 12 h (**Figure S3**, Supporting Information). The shear moduli of $LiBH_4$ (~5 GPa) and $LiBO_2$ (30 GPa) are much lower than that of LLZTO (60 GPa),[6b,22] which facilitates the formation of compact coating around LLZTO particles. The amorphous coatings therefore improve the processability of LLZTO particles to obtain compact SSE pellets.

Moreover, it should note that $LiBH_4$ is a fast lithium ion conductor and is electrochemically stable to Li metal,[23,24] favouring the improvement of electrochemical properties of thus-prepared composite electrolytes.

2.2 Ionic conductivity of the LLZTO composite electrolyte.

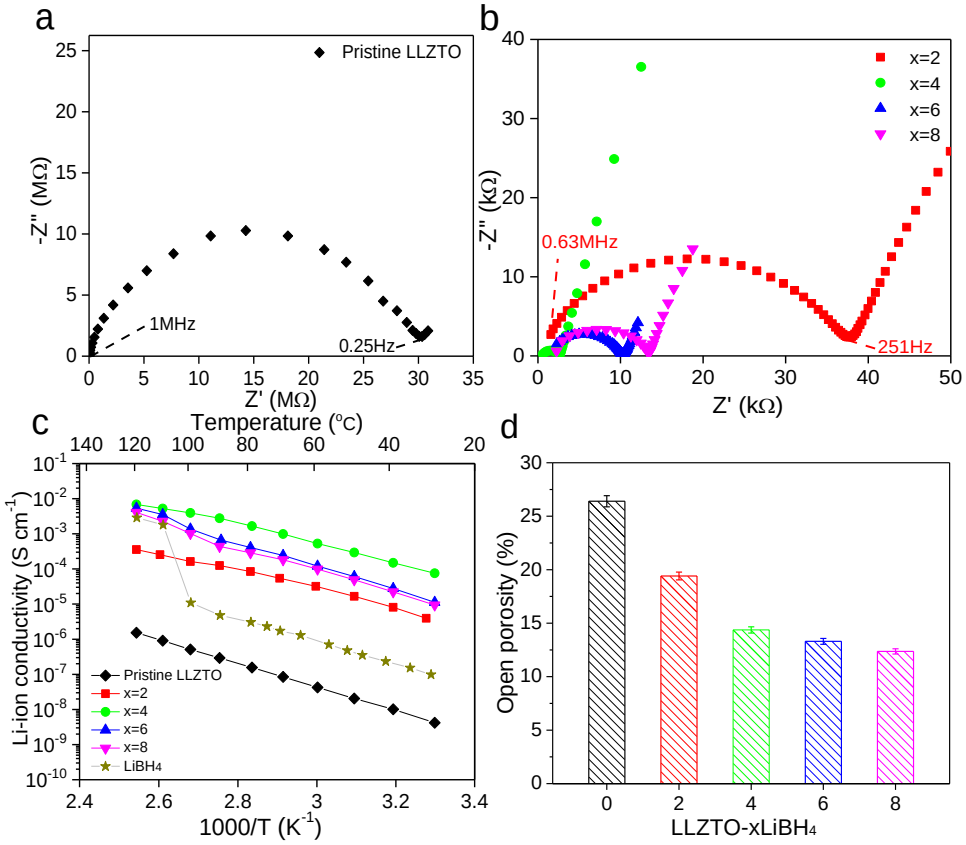

Figure 3. a, b) Nyquist curves, c) Arrhenius plots and d) open porosity of the LLZTO-*x*$LiBH_4$ pellets.

To determine the Li^+ ion conductivity, the as-milled LLZTO-*x*$LiBH_4$ composite was cold pressed into pellets at room temperature and then directly subjected to EIS examination. All the electrochemical impedance spectra (EIS) collected at 30 °C exhibit similar shape composing of a semicircle and a straight line (**Figure 3**a and b), where the semicircle diameter is correlated to resistance associated with grain boundary and pores inside the solid electrolyte (R_{g+p}), and the straight line at low frequency region is related to resistance to ion transfer.[25] Here, the R_{g+p} value of the LLZTO-4$LiBH_4$ sample was determined to be only 2.5 kΩ, in contrast to 30.5 MΩ

for the pristine LLZTO pellet, which means a remarkable improvement in ionic conductivity of LLZTO after ball milled with $LiBH_4$. More interestingly, the 12 h-milled LLZTO-4$LiBH_4$ sample delivered the smallest R_{g+p} value in the present study (**Figure S4**, Supporting Information). This is reasonably related to an optimal combination between the reduced particle size and the surface coating because the ball milling treatment not only initiated the chemical reaction between LLZTO and $LiBH_4$ but also pulverized the LLZTO particles as observed in Figure 1f-k.

The ionic conductivity (σ_{Li+}) was calculated according to the following equation and listed in **Table S1** (Supporting Information).

$$\sigma_{Li+} = \frac{d}{SR_t} \qquad (1)$$

where S is the pellet area, d the thickness and R_t the bulk resistance of the electrolyte pellet. As shown in **Table S1** (Supporting Information), the ionic conductivity of the LLZTO-$x$$LiBH_4$ composite first increases and then decreases with $LiBH_4$ content. The highest Li^+ ion conductivity was obtained for the LLZTO-4$LiBH_4$ sample, which is 8.02×10^{-5} S cm^{-1} at 30 °C. This value is about four orders of magnitude higher than that of pristine LLZTO (4.17×10^{-9} S cm^{-1}) and even approaching to some LLZTO-based SSEs prepared by high-temperature sintering.[26]

Temperature dependence of the ionic conductivities of LLZTO-$x$$LiBH_4$ composites was plotted in **Figure 3**c. There is a good linear relationship between the logarithms of ionic conductivity with the reciprocal of temperatures. The activation energy can be deduced by fitting the plots shown in **Figure 3**c at 30-80 ºC using the Arrhenius equation.

$$\sigma_{Li+} = \left(\frac{A}{T}\right)\exp\left(-\frac{E_a}{kT}\right) \qquad (2)$$

in which A is the pre-exponential factor, E_a is the activation energy, k is the Boltzmann constant and T is the temperature in Kelvin. As shown in **Table S1** (Supporting Information), the E_a

value of the sample at $x = 4$ was calculated to be 0.60 eV, which is apparently lower than that of pristine LLZTO (0.70 eV), suggesting a lower energy barrier for Li^+ ion movement in the $LiBH_4$-modified samples. It should be noted that for samples with $x > 4$, the temperature dependence of the ionic conductivities becomes very similar to that of $LiBH_4$ at elevated temperature, indicating that $LiBH_4$ dominates the electrochemical behavior.

Unlike previous reports, we obtained high Li^+ ion conductivity for the LLZTO-$x$$LiBH_4$ SSE pellets prepared simply by cold pressing without further treatment. To understand the underlying mechanism, open porosity of the SSE pellets was measured. As shown in **Figure 3**d, the presence of $LiBH_4$ effectively reduces the open porosity from 26.4% for pristine LLZTO to 14.4% for the $x = 4$ composite and further to 12.3% for the $x = 8$ composite, which is also evidenced by SEM observation (**Figure 4**a and b). Cavities are clearly visible for pristine LLZTO due to its poor deformability caused by high stiffness,[6b] which leads to point contacts instead of face contacts and therefore restricted Li^+ ion mobility (**Figure 4**c). With the presence of $LiBH_4$, the pellet becomes dense with much reduced cavities. This is likely due to the lower shear moduli of $LiBH_4$ (~5 GPa) and $LiBO_2$ (30 GPa) in comparison with LLZTO (60 GPa),[6b,22] which improve the ductility of particles. Thus, $LiBH_4$ and newly formed $LiBO_2$ are believed to work as a filler and binder to densify the pellets, where more face contacts are established, facilitating Li^+ ion transport between particles (**Figure 4**d). However, too much $LiBH_4$ resulted in a thicker coating, which slows down the Li^+ ion transport between particles,[27] as schematically illustrated in **Figure 4**e. This explains that the optimal Li^+ ion conductivity appears at $x = 4$.

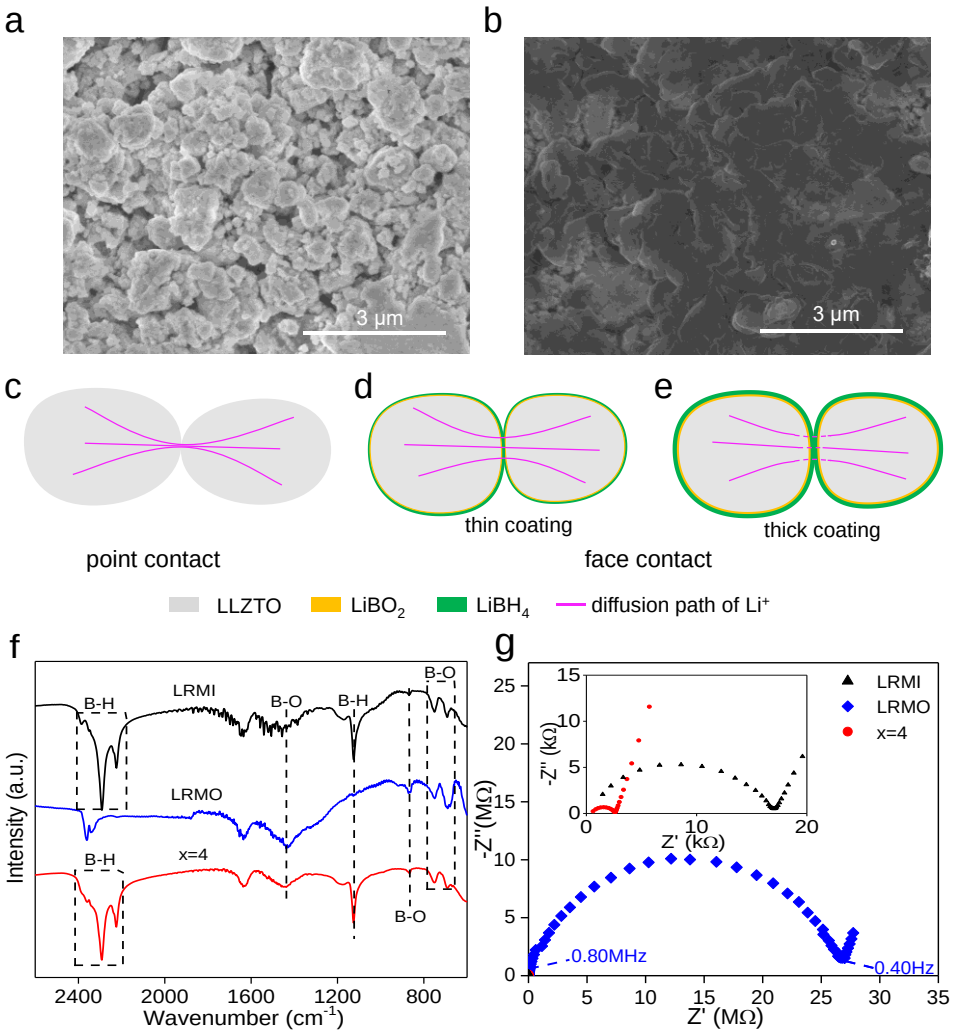

Figure 4. SEM images of pellets of a) pristine LLZTO and b) LLZTO-4$LiBH_4$. Schematic illustration of contact and the Li^+ diffusion path between particles in the pellets of c) pristine LLZTO sample, with d) low and e) high $LiBH_4$ content. f) FTIR spectra and g) Nyquist plots of the LLZTO-4$LiBH_4$ samples with $LiBH_4$ removed (LRMO) and reintroduced (LRMI).

To understand the roles played by $LiBH_4$ and $LiBO_2$, we removed $LiBH_4$ on the surface layer of the as-prepared LLZTO composite using diethyl ether in a glove box. The resultant sample was named as LRMO. After such treatment, the characteristic absorbances of B-H bond in $LiBH_4$ at 2386, 2293, 2226 and 1127 cm^{-1} became absent in the FTIR spectra while those of B-O bond in $LiBO_2$ at 1442, 879, 763 and 692 cm^{-1} were still visible (**Figure 4**f), which confirms the removal of $LiBH_4$. An increased open porosity of 24.95% was observed in the pellet

obtained by cold pressing LRMO under 300 MPa (**Figure S5**, Supporting Information), very close to that of pristine LLZTO, consequently inducing a great decrease in the Li^+ ion conductivity (~ 10^{-9} S cm^{-1}) (**Figure 4**g). Therefore it is $LiBH_4$ rather than $LiBO_2$ playing the role in filling the gap and facilitating ion transfer in the LLZTO-*x*$LiBH_4$ pellets. This conjecture was further confirmed by the fact that the open porosity was reduced (**Figure S3**, Supporting Information) and the Li^+ ion conductivity was recovered again to a value comparable to the x = 4 sample after remixing with a certain amount of $LiBH_4$ (denoted as LRMI), and the bulk resistance (R_{g+p}) was largely reduced from approximately 27 MΩ to 17 kΩ (**Figure 4**g). An additional evidence is that no appreciable change in the bulk resistance was observed when directly ball milling $LiBO_2$ with LLZTO (**Figure S6**, Supporting Information). Here, it should be mentioned that the LRMO sample posses the slightly samller bulk resistance (27 MΩ) with respct to the LLZTO-$LiBO_2$ sample (29 MΩ), indicating a somewhat faster ionic conductivity. This is mainly attributed to the presence of the oxygen vacancies since the LRMO sample mainly consists of the oxygen vacancy-rich LLZTO apart from $LiBO_2$ as mentioned above. However, such imporvement is nearly negligible relative to the enhancement casued by the presence of $LiBH_4$. As for $LiBO_2$, its *in-situ* formation prevents further reaction between $LiBH_4$ and LLZTO during ball milling, consequently resulting in the formation of the $LiBH_4$ outer layer. In addition, the presence of the $LiBO_2$ inner layer is also favorable for avoiding the reaction between $LiBH_4$ and LLZTO during electrochemical charging/discharging by preventing their direct contact as a separation layer, which contributes a stable cyclability as discussed later.

The electronic conductivity of the LLZTO-4$LiBH_4$ composite was further measured on a SUS|SSE|SUS blocking cell by direct current (DC) polarization technique. **Figure 5**a shows the time dependence of current after applying step voltage of 100 mV at 30 ºC. The discharge current first rapidly decreased and then stabilized with time. The electronic conductivity (σ_e) was calculated to be 4.07×10^{-9} S cm^{-1} using the following equation.

$$\sigma_e = \frac{I_0 d}{U_0 S} \qquad (3)$$

where I_0 is the steady current, U_0 is the applied voltage, d is the thickness and S is the area of the SSE pellet. This value is lower than those reported previously (10^{-8} - 10^{-7} S cm^{-1}) for the sintered LLZTO electrolyte pellets,[28] and nearly four orders of magnitude lower than that of Li^+ ion conductivity. The Li^+ transference number was determined to be higher than 0.9999, which has been rarely reported. As a result, the electronic conduction in the $LiBH_4$-modified SSE sample is negligible, which would suppress the growth of Li dendrite and therefore enhance cycling performance.[28b]

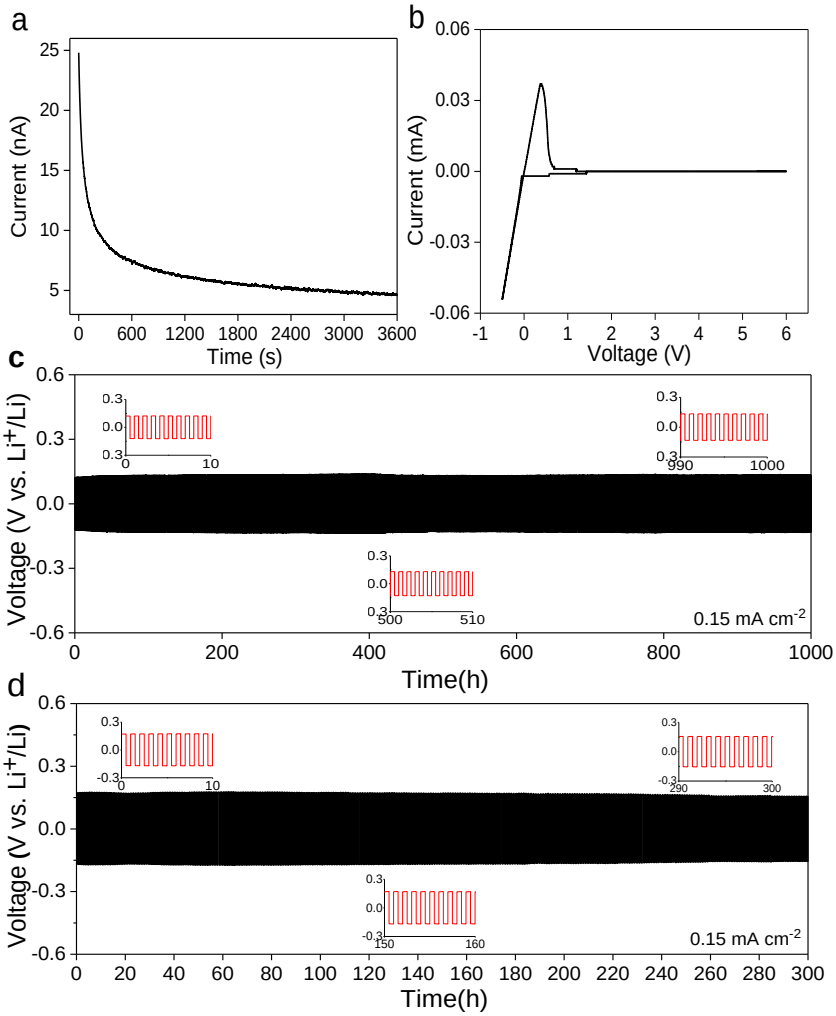

Figure 5. a) DC polarization curve, b) CV curve, and galvanostatic cycling curves at c) 60 ºC and d) 30 ºC of the Li|LLZTO-4$LiBH_4$|Li cells. The insets show the detailed voltage plateau of Li stripping/plating at selected cycles.

2.3 Electrochemical performance of the LLZTO composite electrolyte.

Figure 5b shows the cyclic voltammetry (CV) curve of the SUS|SSE|Li measured at a scan rate of 0.1 mV s^{-1}. It is clear that no additional redox peaks were observed beside the Li plating-stripping peaks between the voltage range of -0.5 V and 6 V, indicating that the $LiBH_4$-modified LLZTO electrolyte was electrochemically stable up to 6 V (vs. Li^+/Li). It was reported that $LiBH_4$ is chemically compatible and electrochemically stable to Li metal with an electrochemical window above 5 V (vs. Li^+/Li).[23,24] The SSE obtained here can therefore be applied to high-voltage solid-state Li and/or Li-ion batteries.

Figure 5c and d show the galvanostatic cycling curve of a Li|LLZTO-4$LiBH_4$|Li cell at a constant current density of 0.15 mA cm^{-2} at 60 ºC and 30 ºC, respectively. Although a Li|LLZTO|Li cell was also assembled and measured under identical conditions for comparison, it nevertheless could not work properly due to the extremely high overpotential (> 5 V even at 0.00015 mA cm^{-2}) caused by the extremely low conductivity of the cold-pressed LLZTO pellets. In contrast, the Li|LLZTO-4$LiBH_4$|Li cell delivered stable and good long-term cycling performance. At 60 ºC, no obvious voltage fluctuations were observed with a low overpotential of 130 mV even after cycling for more than 1000 h. For cycling at 30 ºC, the overpotential slightly increased to 150 mV and the voltage remained still stable after 300 h of cycling. This remarkable cycling performance can be attributed to three factors including the stable surface contact among particles due to the filling of $LiBH_4$ in the pellets, the effective separation between $LiBH_4$ and LLZTO to prevent their reaction and the extremely low electronic conductivity that effectively suppresses the growth of Li dendrite.[28b] As shown in the cross-section SEM images (**Figure 6**a and b), the LLZTO-4$LiBH_4$ composite pellet displays a compact structure, while there are a large number of voids for the pristine LLZTO pellet cold pressing under 300 MPa. Even after cycling for 1000 h at 60 ºC, the $LiBH_4$-modified electrolyte pellet maintains good compactness (**Figure 6**c). In addition, shortening ball milling time induced a poor cycling stability for $LiBH_4$-modified LLZTO (**Figure S7**, Supporting

Information), which is mainly attributed to the occurrence of chemical reaction between $LiBH_4$ and LLZTO during charging/discharging due to their direct contact. This speculation was evidenced by the largely reduced $LiBO_2$ content for the short-time milled samples as characterized by high-resolution B 1s XPS spectra (**Figure S3**, Supporting Information).

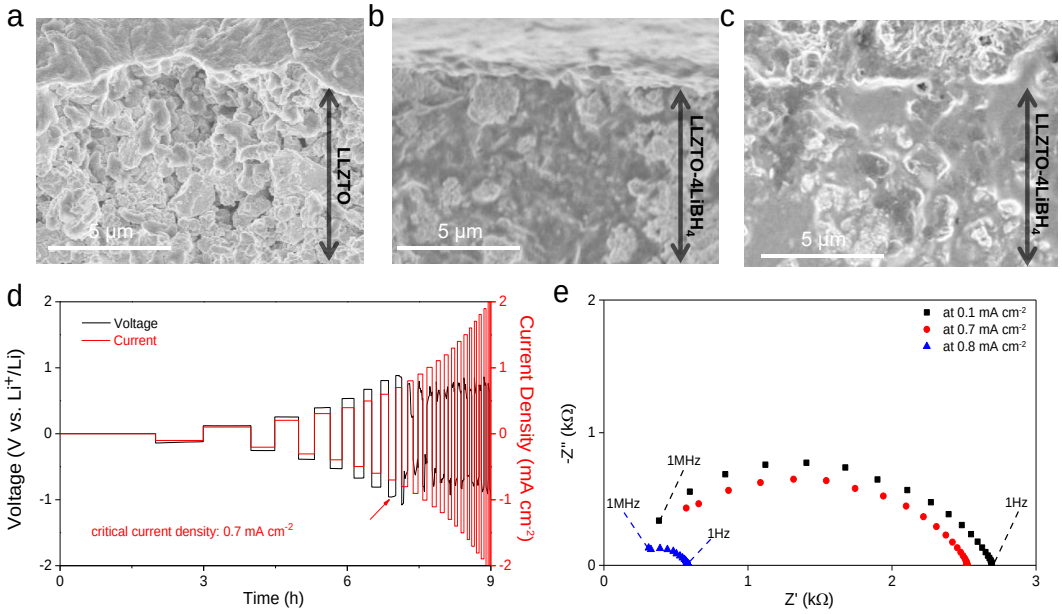

Figure 6. Cross-section SEM images of a) the cold-pressed LLZTO and the LLZTO-4$LiBH_4$ pellet b) before and c) after cycling. d) Stepped current density galvanostatic cycling for the Li|LLZTO-4$LiBH_4$|Li symmetric cell at 30 ºC. e) EIS spectra of the Li|LLZTO-4$LiBH_4$|Li cell after charging/discharging at different current densities during CCD measurement.

Figure 6d presents the cycling curves of Li|LLZTO-4$LiBH_4$|Li at step-wise current densities. The critical current density (CCD) for Li dendrite formation was determined to be 0.7 mA cm^{-2}, which is more than twice the typical garnet-type solid electrolytes (<0.3 mA cm^{-2}).[7] Once the current density was increased over 0.7 mA cm^{-2}, the voltage displayed apparent fluctuations because of the occurrence of local short circuit, as confirmed by EIS measurement **(Figure 6e)**. The impedance semicircle remains nearly unchanged while the current density increased from 0.1 to 0.7 mA cm^{-2}. A dramatic reduction in the semicircle diameter was observed when

operating at 0.8 mA cm^{-2}, indicating a severely decreased resistance due to a local short circuit.[29]

2.4 Full cell performance of the LLZTO composite electrolyte.

To test the compatibility of $LiBH_4$-modified LLZTO composite electrolyte with cathode materials, a full cell of $LiCoO_2$|LLZTO-4$LiBH_4$|Li was constructed and evaluated. The cathode was fabricated by mixing commercial $LiCoO_2$ with SSE at a weight ratio of 7:3 and then uniformly spred over the SSE pellet that is prepared by cold pressing. The charge/discharge curves and the cycling stability are shown in **Figure 7**. The $LiCoO_2$|LLZTO-4$LiBH_4$|Li cell displays a typical high-voltage plateau for charge/discharge (**Figure 7**a). The specific capacity was measured to be 106.5 mAh g^{-1} at a current density of 130 mA g^{-1} for the first cycle with a coulombic efficiency of 85%. The coulombic efficiency increased to 91.5% at the second cycle and further to 95% after 21 cycles. The specific capacity stabilized at 96 mAh g^{-1} after 21 cycles, which corresponds to ~91% of capacity retention, representing a considerable cycling stability. The $LiCoO_2$|LLZTO-4$LiBH_4$|Li full cell was able to power a yellow LED light array as shown in the inset of **Figure 7**b. This preliminary result indicates that $LiBH_4$-modified LLZTO is a promising electrolyte material for ASSLBs. Further investigations to improve the overall properties of ASSLBs using different cathode materials are in progress in our laboratory.

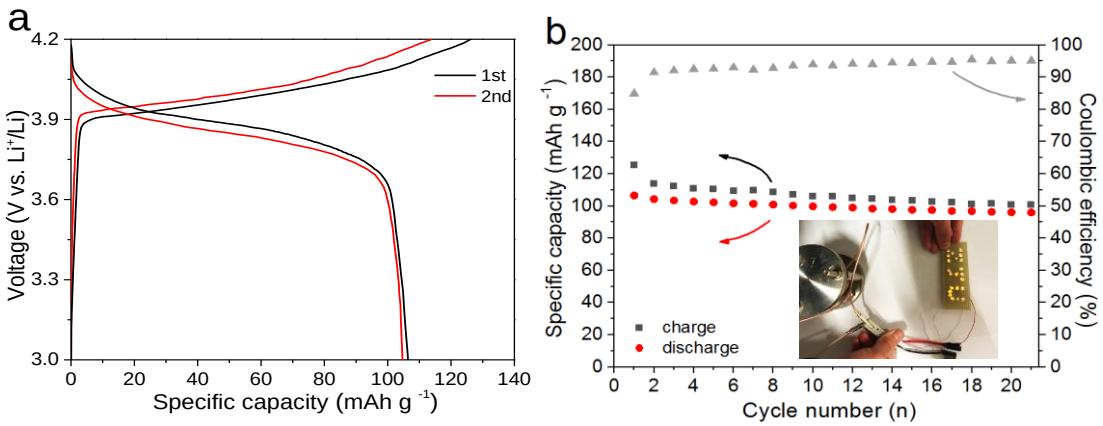

Figure 7. a) Charge/discharge profiles and b) cycling performance of a $LiCoO_2$|LLZTO-4$LiBH_4$|Li full cell. The inset displays a digital photograph of LED array powered by the full

cell.

3. Conclusion

We successfully developed a facile strategy to effectively improve the Li-ion conductivity of LLZTO based solid-state electrolyte. By ball milling LLZTO together with $LiBH_4$, we successfully prepared a dual amorphous layer-coated LLZTO composite with $LiBO_2$ and $LiBH_4$ as the inner and outer layer, respectively. The amorphous coating results in much enhanced contact among particles by playing the roles of filler, binder and bridge. For SSE pellets obtained by a simple cold pressing process, the open porosity of $LiBH_4$-modified LLZTO is less than 50 % of the value for pristine LLZTO. For the $LiBH_4$-modified LLZTO pellets, its Li^+ ion conductivity was measured to be 8.02×10^{-5} S cm^{-1} at 30 ºC, more than four orders of magnitude higher than that of pristine LLZTO (4.17×10^{-9} S cm^{-1}). The pellet also has extremely low electronic conductivity, which would suppress the formation of Li dendrite. Li^+ transference number was determined to be 0.9999, further confirming the exceptionally high Li^+ ion mobility that has been rarely reported. A symmetric Li cell can be cycled for more than 300 h at 0.15 mA cm^{-2} at 30 ºC. The $LiCoO_2$|LLZTO-4$LiBH_4$|Li full cell exhibits a considerable cycling stability with around 100 mAh g^{-1} of capacity, demonstrating great potential of non-sintered LLZTO electrolyte for applications in ASSLBs. With its simplicity in fabrication, this approach can be adopted to improve other oxide-based SSEs. For example, various metal (M=Li, Na, K, Mg) borohydrides can be used to modify different oxide based SSEs for all solid-state batteries (Li/Na/K/Mg based, for instance).

4. Experimental Section

Materials Synthesis. LLZTO (99.99%) and $LiBH_4$ (95%) were purchased from MTI and Acros, respectively. Samples of LLZTO composite with $LiBH_4$ were prepared by ball milling mixtures of LLZTO-*x*$LiBH_4$ (*x* = 0, 2, 4, 6 and 8, molar ratio). Ball milling was performed on a planetary

ball mill (QM-3SP4, Nanjing) at 300 rpm for 12 h. Approximately 1 g of powders were loaded into a milling jar inside an Ar-filled glove box (MBRAUN, Germany). The ball-to-sample weight ratio was kept at 100:1.

Characterization. XRD analysis was performed on a MiniFlex 600 XRD unit (Rigaku, Japan) using Cu K_α radiation (λ = 0.154056 nm) at 40 kV and 15 mA. The 2θ angle was from 10 to 90° with a 0.02° increment. FTIR spectra were recorded with a Bruker Tensor 27 unit (Germany). The sample was mixed with dry KBr powders at a weight ratio of 1:300, and then cold pressed into a pellet for measurement. Microstructure and morphology were characterized using a SU8010 SEM operating at 3 kV and a FEI Tecnai G2 F20 S-TWIN TEM operating at 200 kV coupled with an EDS. XPS analyses were conducted on an ESCALAB 250 Xi spectrometer with Al K_α X-ray source (λ = 0.83401 nm) under a base pressure of 5×10^{-10} Torr. The powder sample was first cold pressed into a pellet inside an argon-filled glove box and then mounted on a sample holder that was transferred in a special transfer vessel from the glove box to the XPS facility to avoid air exposure. Ar ion sputtering was used for depth profile analysis. EPR spectra were obtained at room temperature using a Bruker A300 EPR spectrometer. The open porosity of SSE pellets was measured in n-heptane medium (Sinopharms). The test pellets were outgassed in a suction flask by vacuuming before immersion into n-heptane.

Electrochemical Measurements. For the test cells, stainless steel (SUS) or Li metal electrodes were used to sandwich the SSE, and the assembly was kept in a polyether ether ketone (PEEK) cylinder.[30] The LLZO-*x*$LiBH_4$ SSEs were cold pressed to pellets with 10 mm in diameter and 1-2 mm in thickness. The ionic conductivity of the SSEs was determined by EIS using an Ivium Vertex electrochemical workstation (the Netherlands) in the frequency range of 1 MHz - 1 Hz. DC polarization was conducted by applying a constant voltage of 100 mV for 3600 s. The electrochemical window was examined by performing CV on SUS|SSE|Li cells from -0.5 V to 6 V at a scan rate of 0.1 mV s^{-1}. The galvanostatic plating-stripping cycling was tested on Li|SSE|Li symmetric cells using Neware battery test systems (CT-3008W-5V20A-S4,

Shenzhen, China). CCD was determined by cycling at elevated current densities. The $LiCoO_2$|LLZO-4$LiBH_4$|Li full cells were assembled and tested from 3.0 to 4.2 V. Approximately 10 mg of cathode powder was prepared by mixing $LiCoO_2$ with SSE at a weight ratio of 7:3.

Supporting Information
Supporting Information is available from the Wiley Online Library or from the author.

Acknowledgements

We gratefully acknowledge the financial support from the National Natural Science Foundation of China (52071285 and 51831009) and the National Youth Top-Notch Talent Support Program. Z.H. is the recipient of an Australian Research Council Future Fellowship (project number FT190100658).

Received: ((will be filled in by the editorial staff))
Revised: ((will be filled in by the editorial staff))
Published online: ((will be filled in by the editorial staff))

References

[1] a) J. M. Tarascon, M. Armand, *Nature*, **2001**, *414*, 359-367; b) S. Chu, A. Majumdar, *Nature* **2012**, *488*, 294-303; c) Y. Cao, M. Li, J. Lu, J. Liu, K. Amine, *Nat. Nanotechnol.* **2019**, *14*, 200-207; d) Y. Yang, X. Qu, X. Zhang, Y. Liu, J. Hu, J. Chen, M. Gao, H. Pan, *Adv. Mater.* **2020**, *32*, 1908285.

[2] a) Y. S. Hu, *Nat. Energy* **2016**, *1*, 16042; b) E. Quartarone, P. Mustarelli, *Chem. Soc. Rev.* **2011**, *40*, 2525-2540; c) J. Betz, G. Bieker. P. Meister, T. Placke, M. Winter, R. Schmuch, *Adv. Energy Mater*. **2019**, *9*, 1803170; d) F. Han, J. Yue, C. Chen, N. Zhao, X. Fan, Z. Ma, T. Gao, F. Wang, X. Guo, C. Wang, *Joule* **2018**, *2*, 497-508.

[3] a) K. Fu, Y. Gong, G. T. Hitz, D. W. McOwen, Y. Li, S. Xu, Y. Wen, L. Zhang, C. Wang, G. Pastel, J. Dai, B. Liu, H. Xie, Y. Yao, E. D. Wachsman, L. Hu, *Energy Environ. Sci.* **2017**, *10*, 1568-1575; b) A. Manthiram, X. Yu, S. Wang, *Nat. Rev. Mater.* **2017**, *2*, 16103; c) J. Cuan, Y. Zhou, T. Zhou, S. Ling, K. Rui, Z. Guo, H. Liu, X. Yu, *Adv. Mater*. **2019**,

31, 1803533; d) X. Han, Y. Gong, K. Fu, X. He, G. T. Hitz, J. Dai, A. Pearse, B. Liu, H. Wang, G. Rubloff, Y. Mo, V. Thangadurai, E. D. Wachsman, L. Hu, *Nat. Mater*. **2017**, *16*, 572-580.

[4] a) C. Wang, K. Fu, S. P. Kammampata, D. W. McOwen, A. J. Samson, L. Zhang, G. T. Hitz, A. M. Nolan, E. D. Wachsman, Y. Mo, V. Thangadurai, L. Hu, *Chem. Rev.*, **2020**, 120, 4257-4300; b) L. Xu, J. Li, W. Deng, H. Shuai, S. Li, Z. Xu, J. Li, H. Hou, H. Peng, G. Zou, X. Ji, *Adv. Energy Mater.* **2020**, 2000648; c) N. Zhao, W. Khokhar, Z. Bi, C. Shi, X. Guo, L. Z. Fan, C. W. Nan, *Joule* **2019**, 3, 1190-1199; d) W. L. Huang, N. Zhao, Z. J. Bi, C. Shi, X. X. Guo, L. Z. Fan, C. W. Nan, *Mater. Today Nano*, **2020**, 10, 100075.

[5] a) Y. Zhong, Y. Xie, S. Hwang, Q. Wang, J. J. Cha, D. Su, H. Wang, *Angew. Chem. Int. Ed.* **2020**, 59, 14003-14008; b) Y. Li, J. T. Han, C. A. Wang, H. Xie, J. B. Goodenough, *J. Mater. Chem.* **2012**, 22, 15357-15361; c) Y. Chen, E. Rangasamy, C. D. Lang, K. An, *Chem. Mater.* **2015**, 27, 5491-5494.

[6] a) Y. Kato, S. Hori, T. Saito, K. Suzuki, M. Hirayama, A. Mitsui, M. Yonemura, H. Iba, R. Kanno, *Nat. Energy*, 2016, 1, 16030; b) S. Yu, R. D. Schmidt, R. Garcia-Mendez, E. Herbert, N. J. Dudney, J. B. Wolfenstine, J. Sakamoto, D. J. Siegel, *Chem. Mater.* **2016**, *28*, 197-206. c) Y. Lu, X. Huang, Y. Ruan, Q. Wang, R. Kun, J. Yang, Z. Wen, *J. Mater. Chem. A* **2018**, *6*, 18853-18858; d) W. Feng, X. Dong, X. Zhang, Z. Lai, P. Li, C. Wang, Y. Wang, Y. Xia, *Angew. Chem. Int. Ed.* **2020**, 59, 5346-5349.

[7] a) R. Chen, Q. Li, X. Yu, L. Chen, H. Li, *Chem. Rev.* **2020**, 120, 6820−6877; b) Z. Zhang, L. Zhang, C. Yu, X. Yan, B. Xu, L. M. Wang, *Electrochem. Acta*, **2018**, 289, 254-263.

[8] a) M. Dirican, C. Yan, P. Zhu, X. Zhang, *Mater. Sci. Eng. R* **2019**, 136, 27–46; b) W. Li, C. Sun, J. Jin, Y. Li, C. Chen, Z. Wen, *J. Mater. Chem. A* **2019**, 7, 27304-27312.

[9] H. Xie, C. Li, W. H. Kan, M. Avdeev, C. Zhu, Z. Zhao, X. Chu, D. Mu, F. Wu, *J. Mater. Chem. A* **2019**, *7*, 20633-20639.

[10] S. Zhang, H. Zhao, J. Wang, T. Xu, K. Zhang, Z. Du, *Chem. Eng. J.* **2020**, *393, 124797*.

[11] X. Huang, C. Shen, K. Rui, J. Jin, M. Wu, X. Wu, Z. Wen, *JOM* **2016**, *68*, 2593-2600.

[12] X. Peng, K. Huang, S. Song, F. Wu, Y. Xiang, X. Zhang, ChemElectroChem **2020**, 7, 2389-2394;

[13] T. Jiang, P. He, G. Wang, Y. Shen, C. W. Nan, L. Z. Fan, Adv. Energy Mater. **2020**, 10, 1903376.

[14] Y. Tian, F. Ding, H. Zhong, C. Liu, Y.-B. He, J. Liu, X. Liu, Q. Xu, *Energy Storage Mater.* **2018**, *14*, 49-57.

[15] J. Wolfenstine, J. L. Allen, J. Read, J. Sakamoto, *J. Mater. Sci.* **2013**, *48*, 5846-5851.

[16] H.-S. Kim, J. B. Cook, H. Lin, J. S. Ko, S. H. Tolbert, V. Ozolins, B. Dunn, *Nat. Mater.* **2017**, *16*, 454-460.

[17] a) Y. Zhou, Y. Liu, W. Wu, Y. Zhang, M. Gao, H. Pan, *J. Phys. Chem. C* **2012**, 116, 1588–1595; b) P. Plerdsranoy, D. Kaewsuwan, N. Chanlek, R. Utke, Int. J. Hydrogen Energy, **2017**, 42, 6189-6201.

[18] K. Alexander, E. Tobschal, P. Heitjans, *Z. Phys. Chem.* **2009**, *223*, 1359-1377.

[19] E. Deprez, M. A. Muñoz-Márquez, M. C. Jimenez de Haro, F. J. Palomares, F. Soria, M. Dornheim, R. Bormann, A. Fernández, *J. Appl. Phys.* **2011**, *109*, 014913.

[20] D. A. Hensleyh, S. H. Garofalini, *Appl. Surface Sci.* **1994**, *81*, 331-339.

[21] L. Cheng, E. J. Crumlin, W. Chen, R. Qiao, H. Hou, S. Franz Lux, V. Zorba, R. Russo, R. Kostecki, Z. Liu, K. Persson, W. Yang, J. Cabana, T. Richardson, G. Chen, M. Doeff, *Phys. Chem. Chem. Phys.* **2014**, *16*, 18294-18300.

[22] a) Z. Lu, F. Ciucci, Chem. Mater. 2017, 29, 9308-9319; b) Y. M. Basalaev, E. S. Boldyreva, E. B. Duginova, Russ. Phys. J. 2019, 61, 1868-1875.

[23] M. Matsuo, S. Orimo, *Adv. Energy Mater.* **2011**, *1*, 161-172

[24] a) F. Mo, J. Ruan, S. Sun, Z. Lian, S. Yang, X. Yue, Y. Song, Y. N. Zhou, F. Fang, G. Sun, S. Peng, D. Sun, *Adv. Energy Mater.* **2019**, 9, 1902123; b) K. Kisu, S. Kim, H. Oguchi, N. Toyama, S. Orimo, *J. Power Sources* **2019**, *436*, 226821.

[25] S. Kumazaki, Y. Iriyama, K.-H. Kim, R. Murugan, K. Tanabe, K. Yamamoto, T. Hirayama, Z. Ogumi, *Electrochem. Commun.* **2011**, *13*, 509-512.

[26] a) H. Buschmann, S. Berendts, B. Mogwitz, J. Janek, *J. Power Sources* **2012**, *206*, 236-244; b) K. Tadanaga, R. Takano, T. Ichinose, S. Mori, A. Hayashi, M. Tatsumisago, *Electrochem. Commun.* **2013**, *33*, 51-54.

[27] A. Mei, X. Wang, Y. Feng, S. Zhao, G. Li, H. Geng, Y. Lin, C. Nan, *Solid State Ionics* **2008**, *179*, 2255-2259.

[28] a) Y. Li, Y. Cao, X. Guo, *Solid State Ionics* **2013**, *253*, 76-80; b) F. Han, A. S. Westover, J. Yue, X. Fan, F. Wang, M. Chi, D. N. Leonard, N. J. Dudney, H. Wang, C. Wang, *Nat. Energy* **2019**, *4*, 187-196.

[29] T. Deng, X. Ji, Y. Zhao, L. Cao, S. Li, S. Hwang, C. Luo, P. Wang, H. Jia, X. Fan, X. Lu, D. Su, X. Sun, C. Wang, J. G. Zhang, *Adv. Mater.* **2020**, *32*, 2000030.

[30] H. Liu, Z. Ren, X. Zhang, J. Hu, M. Gao, H. Pan, Y. Liu, *Chem. Mater.* **2020**, *32*, 671-678.

A unique amorphous dual layer-coated LLZTO composite with $LiBO_2$ as the inner layer and $LiBH_4$ as the outer layer was successfully fabricated by a facile mechanochemical process. This novel non-sintered composite electrolyte features high Li-ion conductivity and high Li transference number, and enables long-term cyclability of symmetric Li-Li cells at ambient temperature.

Keywords: energy storage materials, rechargeable Li batteries, solid state electrolyte, borohydrides, LLZTO

Yuan Gao, Shuyang Sun, Xin Zhang, Yongfeng Liu, Jianjiang Hu, Zhenguo Huang, Mingxia Gao, and Hongge Pan*

Amorphous Dual-layer Coating: Enabling High Li-ion Conductivity of Non-sintered Garnet-type Solid Electrolyte

ToC figure

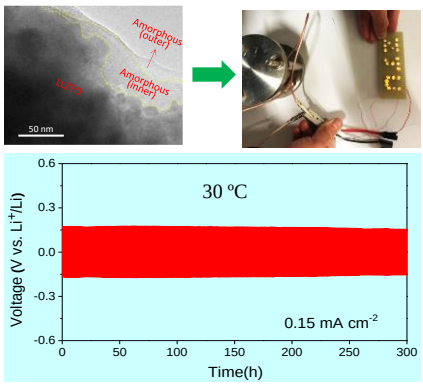

Copyright WILEY-VCH Verlag GmbH & Co. KGaA, 69469 Weinheim, Germany, 2018.

Supporting Information

Amorphous Dual-layer Coating: Enabling High Li-ion Conductivity of Non-sintered Garnet-type Solid Electrolyte

Yuan Gao, Shuyang Sun, Xin Zhang, Yongfeng Liu, Jianjiang Hu, Zhenguo Huang, Mingxia Gao, and Hongge Pan*

Table S1. Ionic conductivity and E_a values of the LLZTO-*x*$LiBH_4$ samples.

Samples	σ_{Li+} (S cm^{-1})	E_a (eV)
Pristine LLZTO	4.17×10^{-9}	0.70
LLZTO-2$LiBH_4$	3.94×10^{-6}	0.67
LLZTO-4$LiBH_4$	8.02×10^{-5}	0.60
LLZTO-6$LiBH_4$	1.12×10^{-5}	0.62
LLZTO-8$LiBH_4$	9.42×10^{-6}	0.63

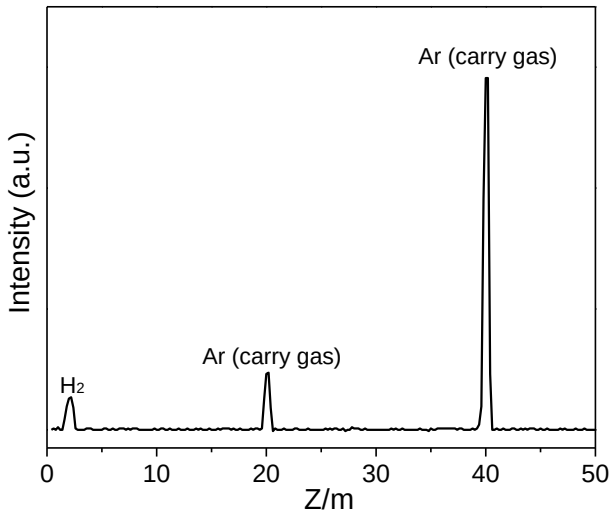

Figure S1. MS signal of gaseous products obtained from the mechanochemical reaction between LLZTO and $LiBH_4$.

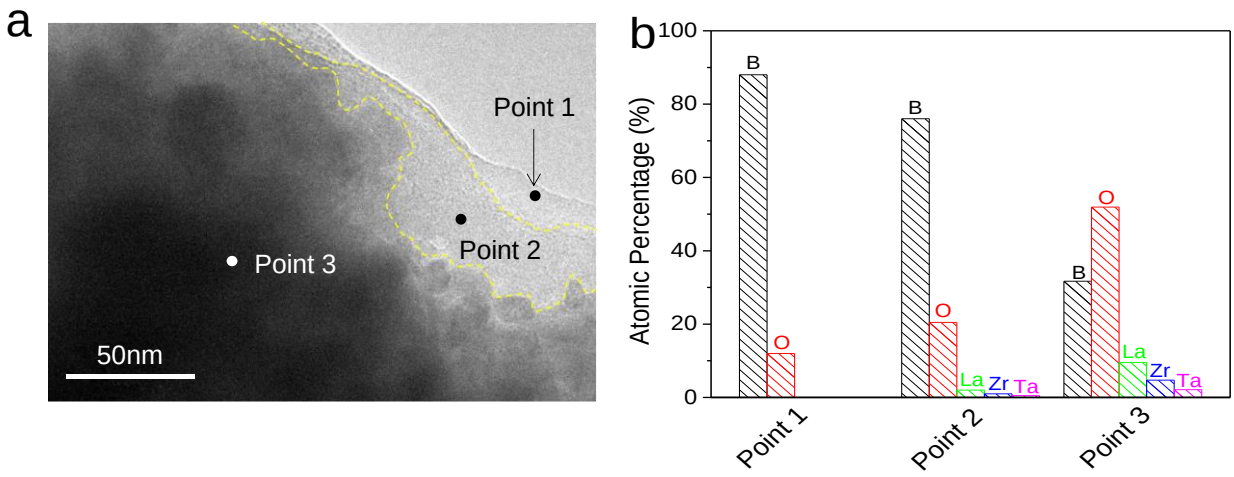

Figure S2. TEM image of the LLZTO-4LiBH$_4$ sample (a) and corresponding atomic compositions of point 1, 2 and 3 (b).

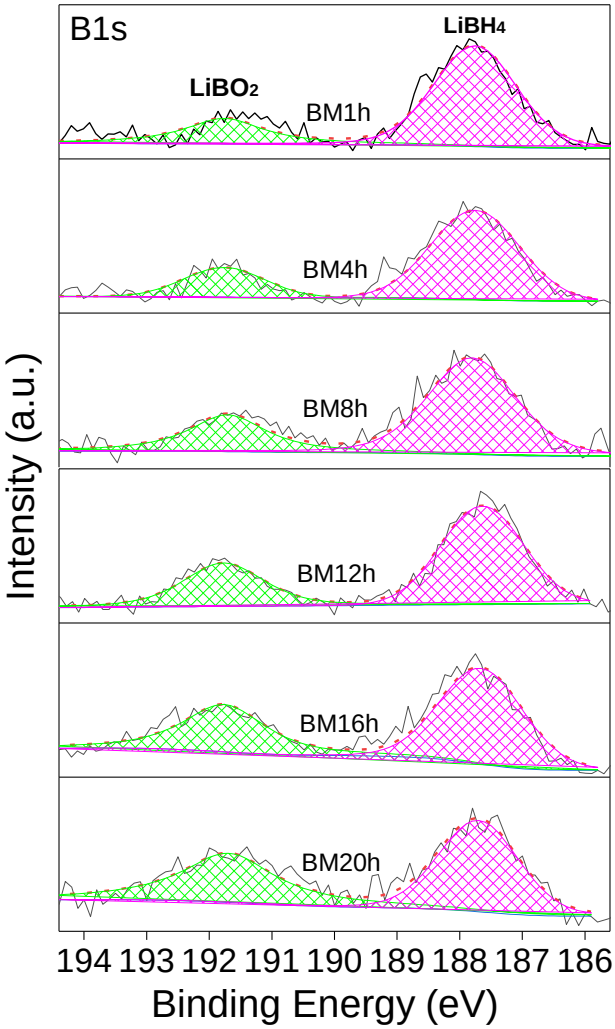

Figure S3. High resolution XPS spectra of B 1s of the LLZTO-4LiBH$_4$ sample milled for times.

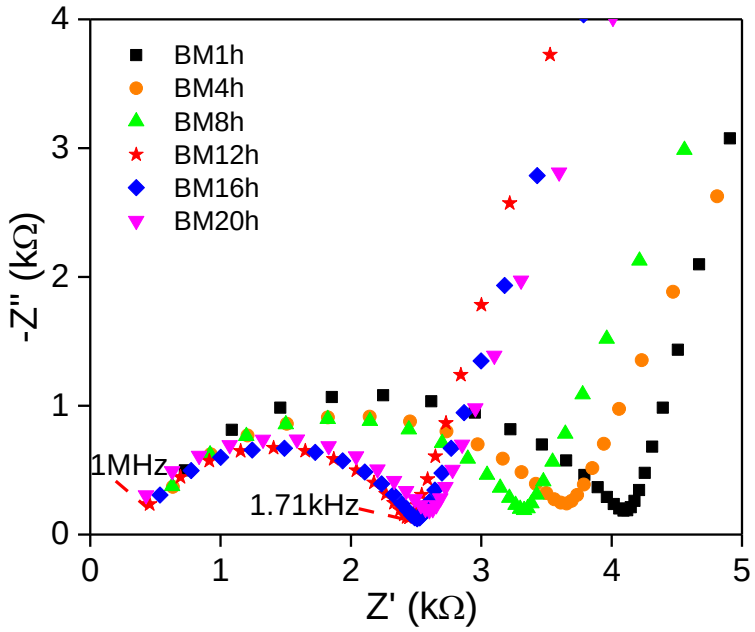

Figure S4. EIS curves of the LLZTO-4LiBH$_4$ sample milled for different times.

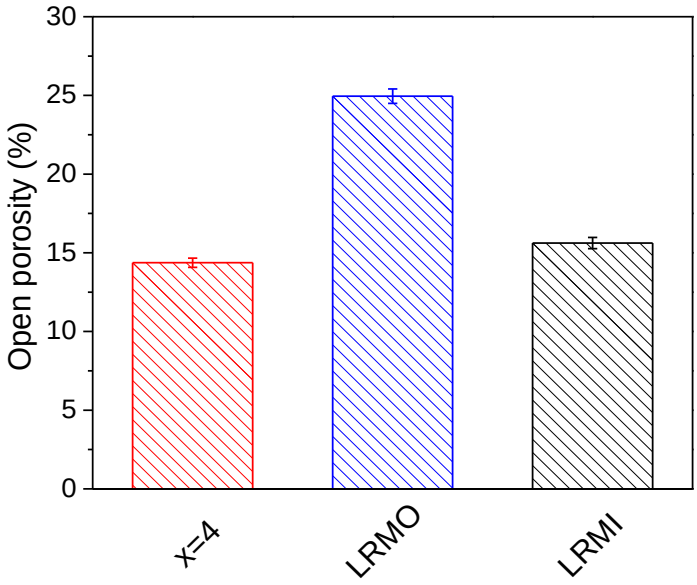

Figure S5. Open porosity of the LLZTO-4LiBH$_4$ sample after different treatments.

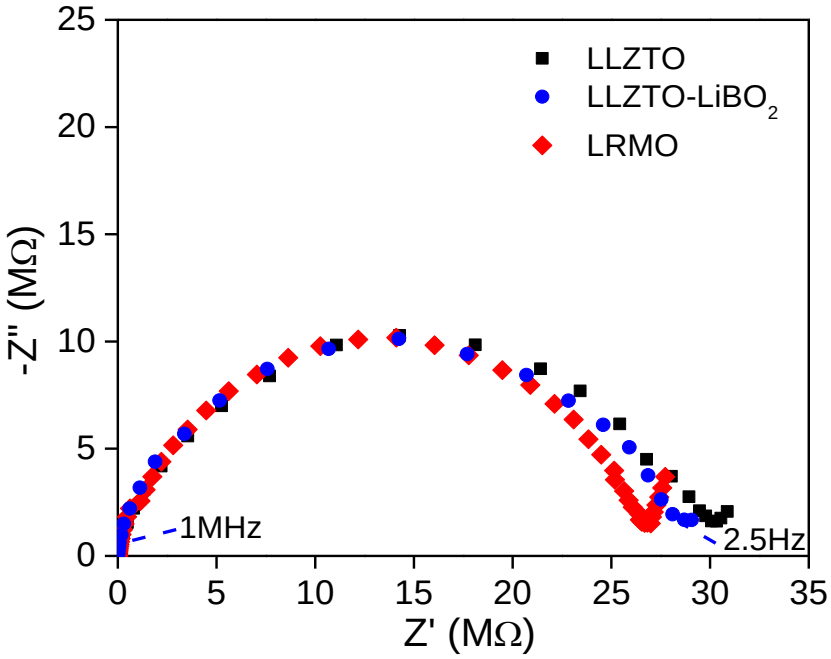

Figure S6. EIS curves of LLZTO, LLZTO-$LiBO_2$ and LMRO samples.

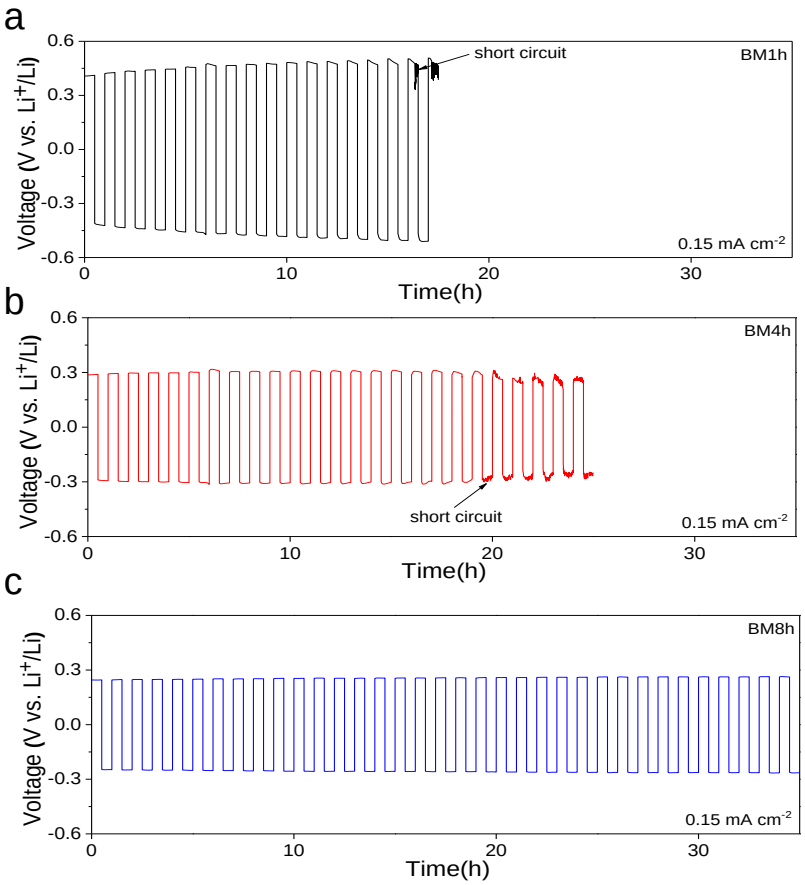

Figure S7. Galvanostatic cycling curves of the Li symmetric cells with LLZTO-4$LiBH_4$ milled for different times.